A railway local degraded adhesion model including variable friction, energy dissipation and adhesion recovery

A railway local degraded adhesion model including variable friction, energy dissipation and adhesion recovery

Martina Meacci, Zhiyong Shi, Elisa Butini, Lorenzo Marini, Enrico Meli, and Andrea Rindi

Department of Industrial Engineering, University of Florence, Florence, Italy

via S. Marta n. 3, 50139 Florence, Italy, e-mail: martina.meacci@unifi.it

A railway local degraded adhesion model including variable friction, energy dissipation and adhesion recovery

The modelling of the wheel-rail contact is fundamental in the railway field since the contact forces directly affect wear, vehicle dynamics and safety. The development of a realistic adhesion model able to describe degraded adhesion conditions is still an open problem, because of the difficulty on obtaining a realistic adhesion law due to the complex non-linear behaviour of the adhesion coefficient. To obtain higher accuracy on the wheel-rail contact model, an innovative degraded adhesion model has been developed, taking complex phenomena including large sliding at the contact interface, energy dissipation and adhesion recovery into consideration. A new approach based on FASTSIM algorithm and Polach theory to solve the tangential contact problem has been specifically designed for the wheel-rail contact and multibody vehicle models. The simulated results have been validated by the comparison with experimental results.

Keywords: Adhesion, wheel-rail contact, multibody modelling, railway vehicles

1. **Introduction**

The accurate modelling of the wheel-rail contact plays a fundamental role in the railway field since the contact forces heavily affect wear, vehicle dynamics and vehicle safety. Typically, simplified and efficient multibody contact models are expected to achieve three main objectives: the contact point detection, the normal problem solution, and the tangential problem solution, including the adhesion model. The contact point detection allows the calculation of the contact point position on the wheel and rail surfaces. The general approaches make use of constraint equations [1], or analytical methods aimed at reducing the algebraic problem dimension [2-4]. The normal problem solution is generally based on Lagrange multipliers [5, 6] and on improved Hertz theory [7-9]. Concerning the solution of the tangential problem, different approaches have been taken into account in the last decades. The most significant strategies comprise the linear

Kalker theory (saturated according to Johnson-Vermulen formula [10-13]), the non linear Kalker theory implemented in the FASTSIM algorithm [13-16], and Polach theory [17, 18] that allows to describe the decrease of the adhesion coefficient with increasing creepage (excluding the contact spin) and to better fit the experimental data. The tangential problem is particularly challenging because of the difficulty to obtain a realistic adhesion law, due to the complex non-linear behaviour of the adhesion coefficient and the presence of external unknown contaminants (third body layer). This is especially true when the degraded adhesion yields a high energy dissipation and, consequently, an adhesion recovery. In the past, the authors developed a preliminary degraded adhesion with the aim of extending the Polach approach. This approximated model was global, i.e. the local behaviour of the contact pressures inside the contact area was neglected [19]. During the years, many studies have been performed to investigate the role of the third body between the contact surfaces, and many analyses have been carried out through both laboratory test rigs and on-track railway tests [20-27]. At the same time phenomena as the dissipation of energy and the adhesion recovery has begun to be more accurately studied, in order to have a better understanding of the non-linear behaviour of the degraded adhesion [28- 30].

The new model proposed by the authors in this work focuses on the main phenomena characterising the degraded adhesion, paying particular attention to the energy dissipation at the contact interface, the consequent cleaning effect and the resulting adhesion recovery due to the removal of external unknown contaminants. This phenomenon is caused by the high energy dissipation on the contact surfaces and by the consequent cleaning effect due to friction. The final adhesion recovery caused by the removal of external contaminants may deeply affect both the vehicle dynamics and the traction and braking manoeuvres. Besides, since most of the physical characteristics of the contaminants are totally unknown in practice, the followed approach will have to minimize the number of hardly measurable physical quantities required by the model.

The model here proposed is local (pressure and slip are locally calculated inside the discretized contact surface), and has been expected to consider the main scenarios of the railway field, e.g. to different wheel and rail profiles, generic railway track and multiple contact points. As railway dynamic simulations are usually carried out by means of multibody models, the contact models have to be suitable to be implemented directly online and in real time within the multibody software (e.g. Matlab-Simulink or Simpack environments), and so they have to guarantee a good accuracy and a high numerical efficiency. For this reason, since the numerical performance is a primary concern, in practice it is impossible to model the contact by considering the wheel and the rail as generic elastic continuous bodies. Finally, the adhesion model has been preliminarily validated through experimental data, showing good accuracy and high numerical efficiency.

In Section 2 the general architecture of the model is explained. In Section 3 the modelling details are described, with particular attention to the tangential problem. Sections 4 and 5 introduce the experimental data and the validation of the new model. The simulation results are presented in Section 6 and conclusions and future developments are proposed in Section 7.

2. General architecture of the model

From a logical point of view, the multibody model consists of two different parts that mutually interact during the dynamical simulation: the 3D model of the railway vehicle and the 3D wheel-rail contact model, as illustrated in Figure 1.

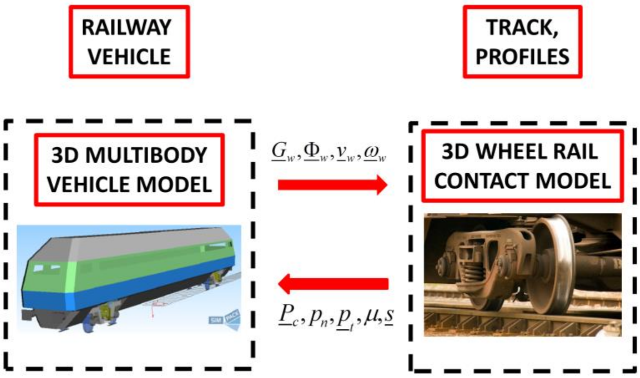

Figure 1. Architecture of the multibody model

At each time step, the multibody vehicle model calculates the kinematic variables of each wheel (position $\underline{G}_w$, orientation $\underline{\Phi}_w$, velocity $\underline{v}_w$ and angular velocity $\underline{\omega}_w$) while the contact model, starting from the knowledge of these quantities, evaluates the normal and tangential contact pressures p_n, $\underline{p}_t$ applied to the wheel into the contact area associated to the contact point $\underline{P}_c$, the sliding $\underline{s}$ in the contact patch and the friction coefficient μ inside the contact area.

Typically, simplified and efficient multibody contact models are characterized by three main submodels: the contact point ($\underline{P}_c$) detection, here based on some innovative procedures recently developed by the authors in previous works [4], [16] [31], the normal problem, solved through the global Hertz theory to evaluate the normal contact pressures ($\underline{p}_n$), and the tangential problem to compute the tangential contact pressure $\underline{p}_t$, the sliding s and the friction coefficient μ(Figure 2). The strategy to solve the tangential problem is based on the local degraded adhesion model developed by the authors in this work. The main inputs of the degraded adhesion model are the wheel kinematic variables, the position $\underline{G}_w$, the orientation $\underline{\Phi}_w$, the wheel velocity $\underline{v}_w$, the wheel angular velocity $\underline{\omega}_w$, the normal pressure at the contact interface p_n and the position of the contact points $\underline{P}_c$. The local degraded adhesion contact model enables the calculation of tangential pressure $\underline{p}_t$, sliding $\underline{s}$ and friction coefficient inside the discretized contact patch by extending the Kalker's FASTSIM algorithm and the Polach theory to properly take into account energy dissipation and adhesion recovery.

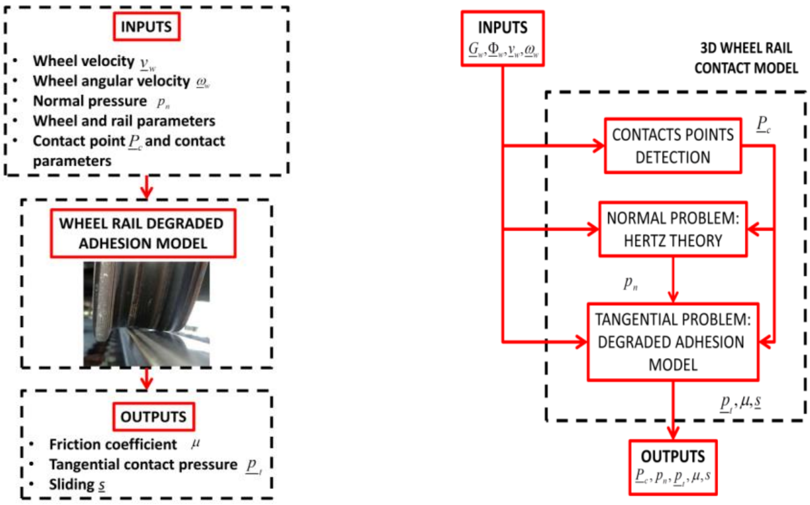

Figure 2. Inputs and outputs of the degraded adhesion model and architecture of the wheel-rail contact model

3. Modelling

This section includes three subsections presenting the modelling details of the adhesion problem, the wheel-rail contact, and the full multibody vehicle accordingly.

3.1 Local adhesion model

The local adhesion model, on which the local tangential contact model is based, is an improvement of the Polach adhesion law [1], [17] and of the FASTSIM algorithm [16], taking into account the energy dissipation at the contact interface and the adhesion recovery (critical phenomena in presence of degraded adhesion). To calculate the local tangential contact variables (tangential contact pressures $\underline{p}_t$ and local sliding $\underline{s}$, all evaluated within the contact patch), the corresponding normal pressures p_n , contact points $\underline{P}_{cw}$, wheel kinematic variables $\underline{G}_w$, $\underline{v}_w$, $\underline{\omega}_w$, and R are set to be known.

A new reference system is defined at the wheel–rail interface on the contact plane (i.e. the common tangent plane between the wheel and rail surfaces): the *x* and *y* axes are the longitudinal and the transversal direction of the contact plane, respectively, while *z* is the normal axis, illustrated as Figure 3.

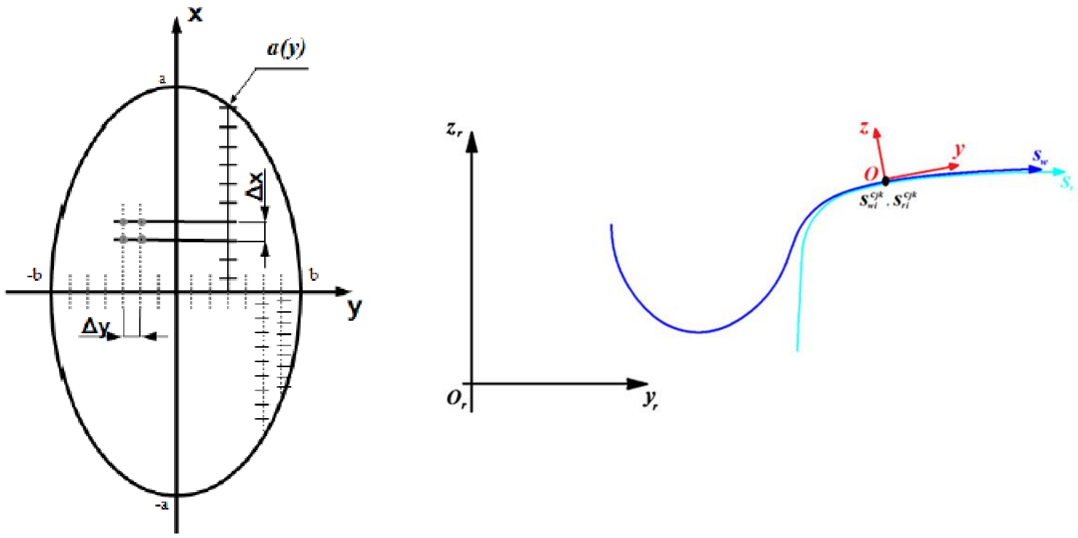

(a). Contact patch discretization (b). Normal abscissa for the wheel and rail profile.

Figure 3. The reference system at the wheel-rail interface

The first step consists in the discretisation of the contact surface: from Hertz theory, the elliptical contact patch and its semi-axes *a* and *b* are discretized in a bidimensional grid (by using a not constant grid resolution) where the quantities p_n, p_t and *s* will be evaluated.

Initially the transversal axis (with respect to the motion direction) of the contact ellipse has been divided in $(n_y - 1)$ equal parts of magnitude Δy by means of n_y equidistant nodes. Then the longitudinal sections of the patch have been divided in $(n_x - 1)$ equal parts of magnitude Δx by means of n_x equidistant nodes, as shown in Figure 3 (a):

$$\Delta y = \frac{2b}{n_y - 1}, \qquad \Delta x(y) = \frac{2a(y)}{n_x - 1} \qquad a(y) = a\sqrt{1 - \frac{y^2}{b^2}} \tag{1}$$

Due to this strategy, the longitudinal grid resolution is not constant but increases near the lateral edges of the ellipse, where the lengths *a(y)* are smaller. This procedure provides more accurate results right next to the edges of the ellipse, where a constant resolution grid would generate excessive numerical noise. The values of the n_x and n_y parameters have to assure the right balance between accuracy and computational load; good values of compromise are in the range 25-50.

The new FASTSIM based algorithm is always based on the proportionality hypothesis between the tangential contact pressure $\underline{p}_t$ and the tangential elastic displacements $\underline{u}_t$, both evaluated within the contact patch [6] [14] [16]:

$$\underline{u}_t(x,y) = L\,\underline{p}_t(x,y) \qquad L = L(\varepsilon, a, b, G, \nu) \tag{2}$$

where the flexibility *L* (function of the global rigid creepages ε, the semi axes of the contact patch *a*, *b*, the wheel and rail combined shear modulus *G* and the wheel and rail combined Poisson's ratio *v*) can be calculated as follows:

$$\begin{gathered} L = \frac{|\varepsilon_x| L_1 + |\varepsilon_y| L_2 + c|\varepsilon_{sp}| L_3}{\left(\varepsilon_x^2 + \varepsilon_y^2 + c^2\varepsilon_{sp}^2\right)^{1/2}} \\ \underline{v}_{pc} = \underline{v}_\omega + \omega_w \times (\underline{P}_c - \underline{G}_w) \\ \varepsilon_x = v_{pcx} / \|\underline{v}_w\| \\ \varepsilon_y = v_{pcy} / \|\underline{v}_w\| \\ \varepsilon_{sp} = \frac{\underline{\omega}_w \cdot \underline{n}}{\|\underline{v}_w\|} \end{gathered} \tag{3}$$

with $L_1 = 8a/(3GC_{11})$, $L_2 = 8a/(3GC_{22})$, $L_3 = \pi a^2/(4GC_{23})$ and $c = \sqrt{ab}$ (the constants C_{ij}, functions both of the Poisson's ratio *v* and of the ratio *a/b*, are the Kalker's parameters and can be found in literature [16]). The local sliding s can be calculated by derivation considering both the elastic creepages and the rigid ones:

$$\underline{s}(x,y) = \underline{\dot{u}}_t(x,y) + V\begin{pmatrix} e_x \\ e_y \end{pmatrix} \tag{4}$$

with

$$\begin{pmatrix} e_x \\ e_y \end{pmatrix} = \begin{pmatrix} \varepsilon_x - y_j \varepsilon_{sp} \\ \varepsilon_y - x_i \varepsilon_{sp} \end{pmatrix} \tag{5}$$

where $V = \|\underline{v}_\omega\|$ is the longitudinal vehicle speed, and e_x, e_y are the rigid local creepages. Once the contact patch is discretized, the FASTSIM algorithm allows the iterative evaluation of both the contact pressures p_n, $\underline{p}_t$ and the local sliding $\underline{s}$ in order to divide the contact patch in adhesion and slip zone. Indicating the generic point of the grid with (x_i, y_j), $1 \le i \le n_x$, $1 \le j \le n_y$, the normal contact pressure can be expressed as:

$$p_n(x_i, y_j) = \frac{3}{2}\frac{N_c}{\pi ab}\sqrt{1 - \frac{x_i^2}{a^2} - \frac{y_j^2}{b^2}} \tag{6}$$

where N_c is the normal contact force, while the limit adhesion pressure $\underline{p}_A$ is:

$$\underline{p}_A(x_i, y_i) = \underline{p}_t(x_{i-1}, y_j) - \begin{pmatrix} e_x \\ e_y \end{pmatrix}\frac{\Delta x(y_i)}{L} \tag{7}$$

Thus, knowing the variable values in the point (x_{i-1},y_j), it is possible to go to the point (x_i,y_j) as follows:

if $\quad \left\|\underline{p}_A(x_i, y_j)\right\| \le \mu(x_i, y_j)\, p_n(x_i, y_j)$

$$\begin{cases} \underline{p}_t(x_i, y_j) = \underline{p}_A(x_i, y_j) \\ \underline{s}(x_i, y_j) = 0 \end{cases} \tag{8}$$

if $\quad \left\|\underline{p}_A(x_i, y_j)\right\| > \mu(x_i, y_j)\, p_n(x_i, y_j)$

$$\begin{cases} \underline{p}_t(x_i, y_j) = \mu(x_i, y_j)\underline{p}_n(x_i, y_j)\underline{p}_A(x_i, y_j) / \left\|\underline{p}_A(x_i, y_j)\right\| \\ \underline{s}(x_i, y_j) = \dfrac{LV}{\Delta x(y_j)}\left[(\underline{p}_t(x_i, y_j) - \underline{p}_A(x_i, y_j)\right] \end{cases} \tag{9}$$

where $\mu(x_i,y_i)$ is the friction coefficient in (x_i,y_i); Eqs. (8) and (9) hold respectively in the adhesion and slip zone. Iterating the procedure for $2 \leq i \leq n_x$ and successively for $1 \leq j \leq n_y$ and assuming as boundary conditions $\underline{p}_t (x_1, y_j) = 0$, $\underline{s} (x_1, y_j) = 0$ for $1 \leq j \leq n_y$ (i.e. stresses and sliding zero out of the contact patch), the desired distribution of $p_n(x_i, y_j)$, $\underline{p}_t(x_i, y_j)$ and $\underline{s}(x_i, y_j)$ can be determined.

In the previous equations the local value of the friction coefficient $\mu(x_i, y_j)$ is still unknown, and has to be modelled. The main phenomena characterising the degraded adhesion are the large sliding occurring at the contact interface and, consequently, the high energy dissipation. Such a dissipation causes a cleaning effect on the contact surfaces and finally an adhesion recovery due to the removal of external contaminants. When the specific dissipated energy W_{sp} is low the cleaning effect is almost absent, the contaminant level h does not change and the friction coefficient μ is equal to its original value in degraded adhesion conditions μ_d. As the energy W_{sp} increases, the cleaning effect increases too, the contaminant level h becomes thinner and the adhesion coefficient μ raises. In the end, for large values of W_{sp}, all the contaminant is removed (h is null) and the adhesion coefficient μ reaches its maximum value μ_r; the adhesion recovery due to the removal of external contaminants is now completed. At the same time if the energy dissipation begins to decrease, due for example to a lower sliding, the reverse process occurs. Figure 4 illustrates the friction coefficient μ as different functions of sliding s in a general situation and in presence of dissipated energy W_{sp} at the contact interface.

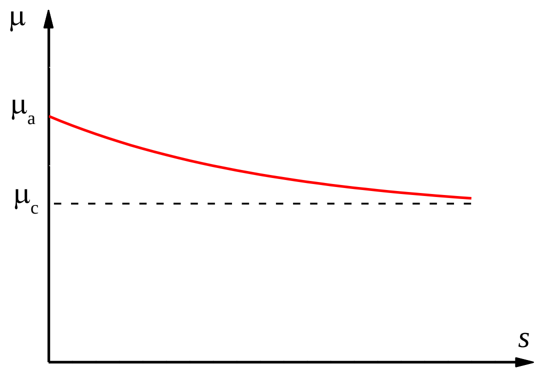

(a). Standard behaviour of the frictional coefficient μ as a function of the sliding s.

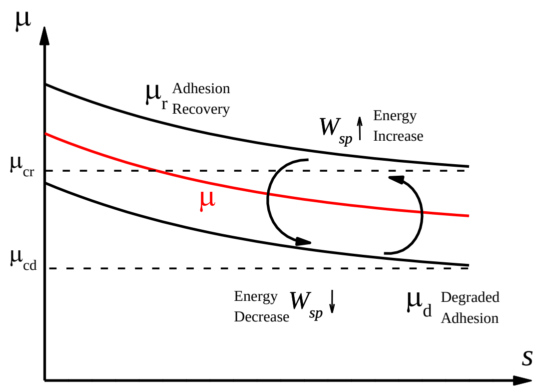

(b). The friction coefficient μ as function of the sliding s in presence of dissipated energy W_{sp} at the contact interface.

Figure 4. The friction coefficient μ as function of sliding s (a) standard and (b) in presence of dissipated energy W_{sp} at the contact interface

Since the contaminant level hand its characteristics are usually totally unknown, it is useful trying to experimentally correlate the friction coefficient μ directly with the specific-dissipated energy W_{sp}. To reproduce the qualitative trend previously described and to allow the friction coefficient to vary between the extreme values μ_d and μ_r, the following expression for μ is proposed:

$$\mu = \left[1 - \lambda(W_{sp})\right]\mu_d + \lambda(W_{sp})\mu_r \qquad (10)$$

where $\lambda(W_{sp})$ is an unknown transition function between degraded adhesion and adhesion recovery. The function $\lambda(W_{sp})$ has to be positive and monotonous increasing; moreover the following boundary conditions are supposed to be verified: $\lambda(0) = 0$ and $\lambda(+\infty) = 1$. This way the authors suppose that the transition between degraded adhesion and adhesion recovery only depends on W_{sp}. This hypothesis is obviously only an approximation but, as it will be clearer in the next chapters, it well describes the adhesion behaviour.

Initially, to catch the physical essence of the problem without introducing a large number of unmanageable and unmeasurable parameters, the authors have chosen the following simple expression for $\lambda(W_{sp})$:

$$\lambda(W_{sp}) = 1 - e^{-\tau|Wsp|} \tag{11}$$

where τ is now the only unknown parameter to be tuned on the base of the experimental data. In this research activity the two main friction coefficients μ_d and μ_r (degraded adhesion and adhesion recovery) have been calculated according to:

$$\begin{cases} \mu_d(x_i\,, y_j) = \left(\dfrac{\mu_{cd}}{A_d} - \mu_{cd}\right) e^{-s(x_{i-1}, y_j)\gamma_d} + \mu_{cd} \\ \\ \mu_r(x_i\,, y_j) = \left(\dfrac{\mu_{cr}}{A_r} - \mu_{cr}\right) e^{-s(x_{i-1}, y_j)\gamma_r} + \mu_{cr} \end{cases} \tag{12}$$

where $s = \|\underline{s}\|$, μ_{cd}, μ_{cr} are the kinematic values of μ_d, μ_r, $\frac{\mu_{cd}}{A_d}, \frac{\mu_{cr}}{A_r}$ are the static values of μ_d, μ_r , and γ_r , γ_d are the parameters that relate the static and the kinematic friction. Consequently, according to what previously written:

$$\begin{cases} \mu(x_i, y_j) = (1-\lambda)\mu_d(x_i, y_j) + \lambda\mu_r(x_i, y_j) \\ \lambda = 1 - e^{-\tau\,|Wsp\,|} \end{cases} \tag{13}$$

The specific dissipated energy W_{sp} can be calculated as:

$$W_{sp}(x_i, y_i) = \underline{p}_A(x_i, y_j) \cdot \underline{s}(x_{i-1}, y_j) \tag{14}$$

This process is repeated for each point of the grid that discretises the contact patch and requires boundary conditions on the points (x_1 , y_j). In particular, sliding $\underline{s}$ and pressures $\underline{p}_t$ on the edge of the contact patch are set equal to zero, while the adhesion coefficients μ_d, μ_r are equal to the static values:

$$\begin{aligned} \underline{s}(x_1, y_j) &= \underline{0} \\ \underline{p}_t(x_1, y_j) &= \underline{0} \end{aligned} \tag{15}$$

$$\begin{cases} \mu_d(x_1, y_j) = \mu_{cd}/A_d \\ \mu_r(x_1, y_j) = \mu_{cr}/A_r \end{cases}$$

$$\mu(x_1, y_j) = \mu_d(x_1, y_j)$$

$$\text{with } W_{sp}(x_1, y_j) = 0$$

Finally it is possible to evaluate the tangential force acting on the contact patch area by integration:

$$\underline{T}_x = \int \underline{p}_{tx} dA$$

$$\underline{T}_y = \int \underline{p}_{ty} dA$$

$$M_{sp} = \int_A (xp_{ty} - yp_{tx}) dA \tag{16}$$

$$\underline{T}_c = T_x \underline{J}_1 + T_y \underline{J}_2$$

$$\underline{M}_{sp} = M_{sp} \underline{n}$$

3.2 Wheel-rail contact model

As introduced in Section 2, the wheel-rail contact model adopt inputs are the kinematic variables of each wheel (position $\underline{G}_w$, orientation $\underline{\Phi}_w$, velocity $\underline{v}_w$ and angular velocity $\underline{\omega}_w$) together with the track geometry and the wheel and rail profiles. The outputs are the normal and tangential contact pressures p_n, $\underline{p}_t$ (applied to the wheel in correspondence of the contact point $\underline{P}_c$), the sliding $\underline{s}$ and the friction coefficient μ. The solutions for contact points detection and the normal problem implemented in this work can be seen in [4], [16], [31]~[33].

3.3 Multibody vehicle model

The mutibody vehicle model has been established to investigate the dynamic behaviour of the vehicle, based on the UIC-Z1 vehicle, provided by Trenitalia s.p.a [35]. Figure 5 shows the operated UIC-Z1 vehicle.

Figure 5. The UIC-Z1 vehicle.

The vehicle is composed of one carbody, two bogie frames, eight axle boxes and four wheelsets. The primary suspension, including flex coil springs (two coaxial helical compression springs), vertical hydraulic dampers and axle box bushings, connects the bogie frame to the four axle boxes while the secondary suspension (vertical lateral and longitudinal ant-yaw dampers, lateral bump-stops, anti-roll bar and traction rod), connects the carbody to the bogie frames.

The multibody vehicle model takes into account all the degrees of freedom (DOFs) of the system bodies, including one carbody, two bogie frames, eight axle boxes, and four wheelsets. Considering the kinematic constraints that link the axle boxes and the wheelsets (cylindrical 1DOF joints) and without including the wheel-rail contacts, the whole system has 50 DOFs.

The wheel thread and rail profile are ORE S 1002 and UIC 60 respectively. Tab.1 lists the main parameters of the railway vehicle. The main inertial properties of the bodies are summarized in Tab. 2. Both the primary suspension (springs, dampers and axle box bushings) and the secondary suspension (springs, dampers, lateral bump-stops, anti-roll bar and traction rod) have been modelled through 3D visco-elastic force elements able to describe all the main non-linearities of the system.

Table 1 Main characteristics of the railway vehicle.

Parameters	**Units**	**Value**
Total mass	[kg]	43000
Bogie wheelbase	[m]	2.56
Bogie distance	[m]	19
Wheel diameter	[m]	0.89

Table 2 Inertial properties of the rigid bodies.

Body	**Mass [kg]**	**I_{xx} [kgm^2]**	**I_{yy} [kgm^2]**	**I_{zz} [kgm^2]**
Carbody	≈ 29000	76400	1494400	1467160
Bogie	≈ 3000	2400	1900	4000
Wheelset	≈ 1300	800	160	800
Axlebox	≈ 200	3	12	12

In Tab. 3 the characteristics of the main linear elastic force elements of both the suspension stages are reported. The non-linear elastic force elements have been modelled through non-linear functions that correlate the displacements and the related velocities of the force elements connection points to the elastic and damping forces exchanged by the bodies. Finally, also the Wheel Slide Protection (WSP) system of the railway vehicle UICZ1 has been modelled to better investigate the vehicle behaviour during the braking phase under degraded adhesion conditions [36]. The whole vehicle model has been implemented in the Matlab-Simulink environment.

Table 3 Main linear elastic characteristics of the two stage suspensions.

Element	**Primary suspension**	**Secondary suspension**	**Axle bushing**	**Anti-roll bar**

Transl. Stiff. x	[N/m]	844000	124000	40000000	0
Transl. Stiff. y	[N/m]	844000	124000	6500000	0
Transl. Stiff. z	[N/m]	790000	340000	40000000	0
Rotat. Stiff. x	[Nm/rad]	10700	0	45000	2500000
Rotat. Stiff. y	[Nm/rad]	10700	0	9700	0
Rotat. Stiff. z	[Nm/rad]	0	0	45000	0

4. Experimental campaign and measured data

The local degraded adhesion model has been validated by means of experimental data provided by Trenitalia s.p.a., coming from on-track tests performed in Velim (Czech Republic) with the coach UIC-Z1, [35] and [36]. The considered vehicle is equipped with a fully-working WSP system. The experimental tests have been carried out on a straight railway track. The wheel profile is the ORE S1002 (with a wheelset width d_w equal to 1.5m and a wheel radius r equal to 0.445m) while the rail profile is the UIC60 (with a gauge d_r equal to 1.435 m and a laying angle equal to 1/20 rad).

Table 4 Main wheel-rail contact characteristics

Parameters	Unit	Value
Young modulus	[Pa]	$2.1*10^{11}$
Shear modulus	[Pa]	$8*10^{10}$
Poisson coefficient	[Ns/m]	0.3
Contact damping constant	-	$1*10^{5}$
Polach reduction factor k_{ad}	-	0.3
Polach reduction factor k_{sd}	-	0.1
Polach reduction factor k_{ar}	-	1.0
Polach reduction factor k_{sr}	-	0.4
Kinetic friction coefficient μ_{cd}	-	0.06

Kinetic friction coefficient μ_{cr}	-	0.28
Friction ratio A_d	-	0.4
Friction ratio A_r		0.4
Friction decrease rate γ_d	[s/m]	0.2
Friction decrease rate γ_r	[s/m]	0.6

In Tab. 4 the main wheel, rail and contact parameters are reported. The value of the kinetic friction coefficient under degraded adhesion conditions μ_{cd} depends on the test performed on the track. According to the current regulations in force, the degraded adhesion conditions are usually reproduced using a watery solution containing surface-active agents, e.g. a solution sprinkled by a specially provided nozzle directly on the wheel-rail interface on the first wheelset in the running direction. The surface-active agent concentration in the solution varies according to the type of test and the desired friction level. The value of the kinetic friction coefficient under full adhesion recovery μ_{cr} corresponds to the classical kinetic friction coefficient under dry conditions. During the experimental campaign, for each test, the following physical quantities have been experimentally measured (with a sample time Δt_s equal to 0.01s):

- the longitudinal vehicle velocity v_v^{sp} . For the sake of simplicity all the longitudinal wheel velocities v_{wj}^{sp} (j represents the *j-th* wheel) are considered equal to v_v^{sp}. The acceleration of the vehicle a_v^{sp} and of the wheels a_{wj}^{sp} can be obtained by derivation and by properly filtering the numerical noise.
- the rotation velocities of all the wheels ω_{wj}^{sp}. The angular accelerations $\dot{\omega}_{wj}^{sp}$ can be calculated by derivation and by properly filtering.
- the vertical loads N_{wj}^{sp} on the wheels. The vertical contact forces N_{cj}^{sp} can be approximately evaluated starting from N_{wj}^{sp} by taking into account the weight of the wheels.

- the traction or braking torques C_{wj}^{sp} applied to the wheels.

By way of example in Figure 6 the wheel longitudinal and rotational velocities v_{w1}^{sp} and $r\omega_{w1}^{sp}$ (first wheelset) are reported for one of the tests of the experimental campaign; both the WSP intervention and the adhesion recovery in the second part of the braking manoeuvre are clearly visible.

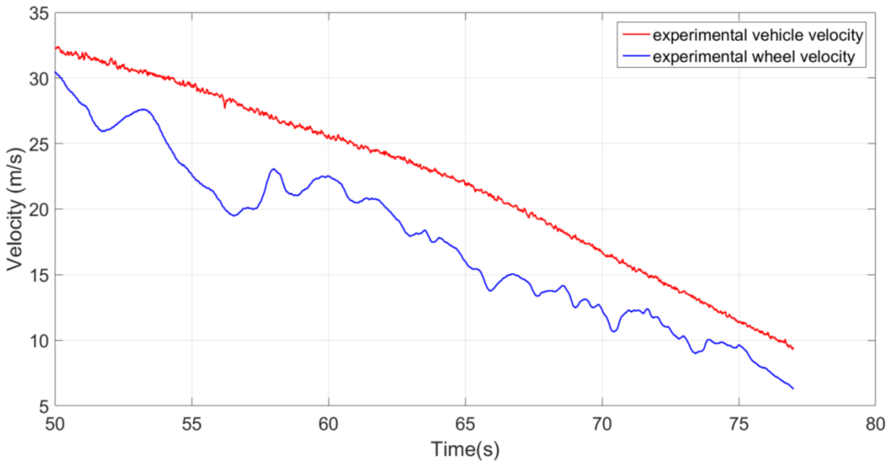

Figure 6. Experimental trend of the vehicle velocity v_{w1}^{sp} and wheel velocity $r\omega_{w1}^{sp}$ for the first wheelset

The chosen simulation starts from a vehicle velocity of $32{,}5\ m/s$ and, after few seconds, a braking torque for each wheelset is applied (as shown in Figure 7). The values of each braking torque are modulated by the WSP during the run of the train depending on the dynamics of the system.

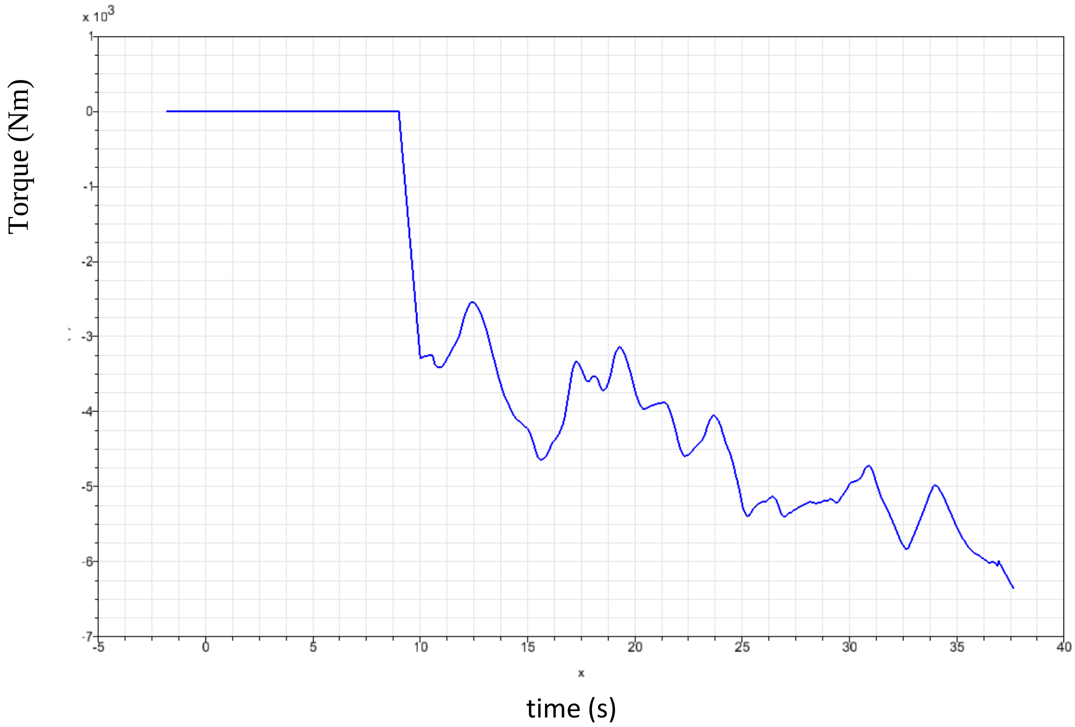

Figure 7. Experimental trend of the braking torque for the first wheelset

5. Preliminary experimental validation of the local adhesion model

In this section, the model described in Section 3 is validated, including the influence of the parameter τ, and the model validation.

5.1 Influence of the parameter τ on the results

In this preliminary phase, the effect of the parameter τ on the dynamics response of the vehicle is investigated.

In Figure 8, the trend of the simulated first wheelset velocity $r\omega_{w1}^{sp}$, varying only the parameter τ is shown. As it can be noticed, the adhesion increases as the parameter τ grows, until the limit condition $\tau = 3 \cdot 10^{-8} \frac{m^2}{W}$, corresponding to a complete (immediate adhesion recovery) adhesion.

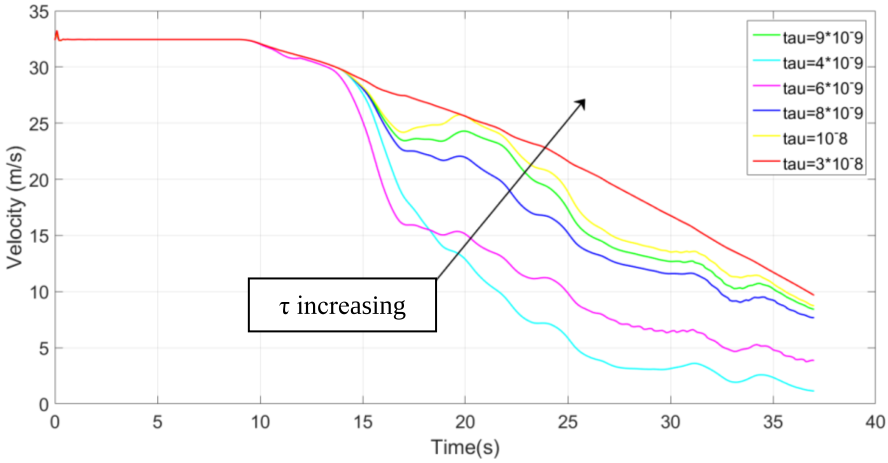

Figure 8. Simulated wheel velocity of the first wheelset $r\omega_{w1}^{sp}$ varying the parameter τ

For these simulations the optimized value chosen for τ has been $\tau = 9 * 10^{-9}$ m^2/W, the one that best reflects the experimental data.

5.2 Model validation

The adhesion model validation is mainly focused on the velocities v_v^{sm}, $r\omega_{wj}^{sm}$; v_v^{sm} is the longitudinal vehicle velocity, ω_{wj}^{sm} is the rotational wheelset velocity and, for the sake of simplicity, *r* is always the nominal wheel radius. These variables have been chosen because they are the most important physical quantities in a braking manoeuvre under degraded adhesion conditions. The variables coming from the 3D multibody model have been compared with the correspondent experimental quantities v_v^{sp}, $r\omega_{wj}^{sp}$. By way of example the time histories of the velocities v_v^{sm}, v_v^{sp} and $r\omega_{w1}$, $r\omega_{w1}^{sp}$, are reported in Figure 9, with a chosen $\tau = 9 \times 10^{-9} m^2/W$.

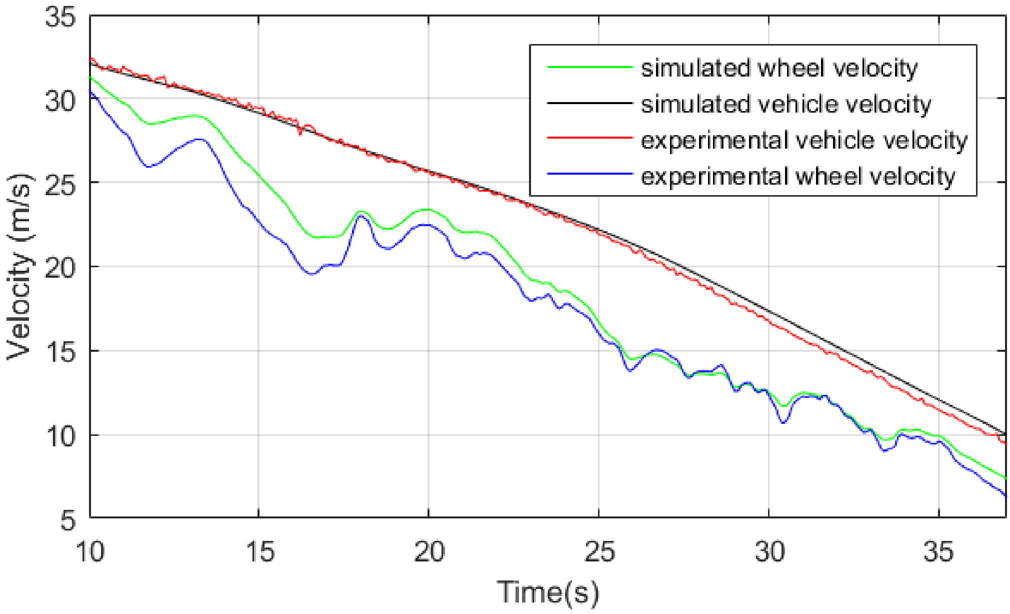

Figure 9. Comparison between the experimental and simulated longitudinal velocities of the vehicle and the first wheelset.

The results of the analysis show a good agreement in terms of translational velocities v_v^{sm}, v_v^{sp}. Concerning the velocities $r\omega_{w1}^{sm}$, $r\omega_{w1}^{sp}$ (and thus the angular velocities) the matching is satisfying. However these physical quantities cannot be locally compared to each other because of the complexity and the chaoticity of the system due, for instance, to the presence of discontinuous and non-linear threshold elements like the WSP. To better evaluate the behaviour of $r\omega_{w1}^{sm}$ and $r\omega_{wj}^{sp}$ from a global point of view, it is useful to introduce the statistical means $\bar{s}_j^{sm}$, $\bar{s}_j^{sp}$ and standard deviations Δ_j^{sm}, Δ_j^{sp} of the calculated sliding s_j^{sm} and of the experimental ones s_j^{sp} :

$$\begin{aligned} s_j^{sm} &= v_v^{sm} - r\omega_{wj}^{sm} \\ s_j^{sp} &= v_v^{sp} - r\omega_{wj}^{sp} \end{aligned} \tag{17}$$

The statistical indices are then evaluated as follows:

$$\bar{s}_j^{sm} = \frac{1}{T_F - T_I}\int_{T_I}^{T_F} s_j^{sm} dt$$
$$\bar{s}_j^{sp} = \frac{1}{T_F - T_I}\int_{T_I}^{T_F} s_j^{sp} dt$$
$$\Delta s_j^{sm} = \sqrt{\frac{1}{T_F - T_I}\int_{T_I}^{T_F} (s_j^{sm} - \bar{s}_j^{sm})^2 dt} \tag{18}$$
$$\Delta s_j^{sp} = \sqrt{\frac{1}{T_F - T_I}\int_{T_I}^{T_F} (s_j^{sp} - \bar{s}_j^{sp})^2 dt}$$

where T_I and T_F are initial and final times of the simulation, respectively. For instance, the means $\bar{s}_1^{sm}$, $\bar{s}_1^{sp}$ and the standard deviations Δs_1^{sm}, Δs_1^{sp} of the slidings s_1^{sm}, s_1^{sp} are summarized in Tab. 5; they confirm the good matching also in terms of sliding and rotational velocities.

Table 5 Statistical comparison between some experimental and simulated sliding s_1^{sp}, s_1^{sm}.

Parameters		Mean	Standard deviation
Adhesion Coefficient	Real f_1^{sp}	0.111	0.0156
	Simulated f_1^{sm}	0.110	0.0098
Sliding [m/s]	Real s_1^{sp}	3.23	1.65
	Simulated s_1^{sm}	3.07	2.70

In Figure 10(a) and table 5 the trend of the experimental and simulated adhesion coefficient $f_j^{sp} = \frac{T_{cj}^{sp}}{N_{cj}^{sp}}$ $f_j^{sim} = \frac{T_{cj}^{sm}}{N_{cj}^{sm}}$ is also shown, where T_{cj}^{sp} and T_{cj}^{sm} are approximately estimated as $I_j^{sm/sp}\dot{\omega}_{wj}^{sm/sp} = C_{wj}^{sm/sp} - T_{cj}^{sm/sp} \cdot r$. Additionally the normal contact forces have been evaluated for the first wheelset, as shown in Figure 10(b), and to have a complete overview of the trend of sliding involved, a comparison between the experimental and simulated sliding has been performed and reported in Figure 10(c).

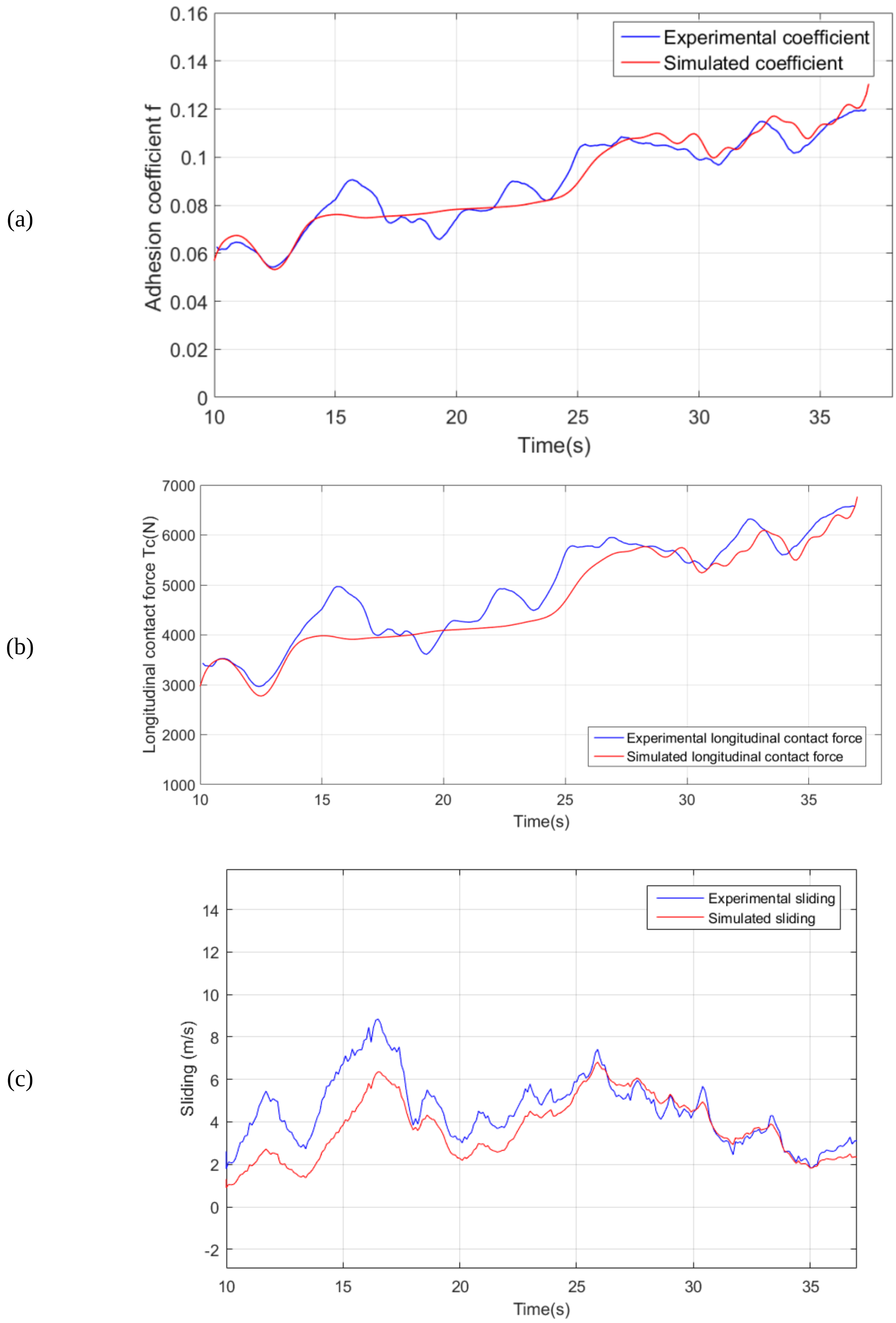

Figure 10. Comparison between the experimental and simulated results for (a) adhesion coefficients f_j^{sp} , f_j^{sm} , (b) longitudinal contact force T_{c1}^{sm} , T_{c1}^{sp} and (c) sliding s_1^{sp} , s_1^{sm}

In conclusion, the numerical simulations of the vehicle dynamics during the braking manoeuvre highlight again the capability of the developed model in approximating the complex and highly non-linear behaviour of the degraded adhesion.

6. Simulation results

A comparison of the local tangential pressures $\underline{p}_t$ in a pure sliding condition (taken at 27s of the simulation) and in a partial adherence condition (taken at 13s when the loss of adherence is starting) is shown in Figure 11. Then, a comparison of the local sliding $\underline{s}$ in a pure sliding and in a partial adherence condition is shown in Figure 12.

Figure 13 illustrates the different distribution of the W_{sp} in the two abovementioned conditions. It is seen that as the W_{sp} is directly connected with the sliding, the value of W_{sp} reaches the maximum in a pure sliding condition, while equals to zero in the presence of adherence.

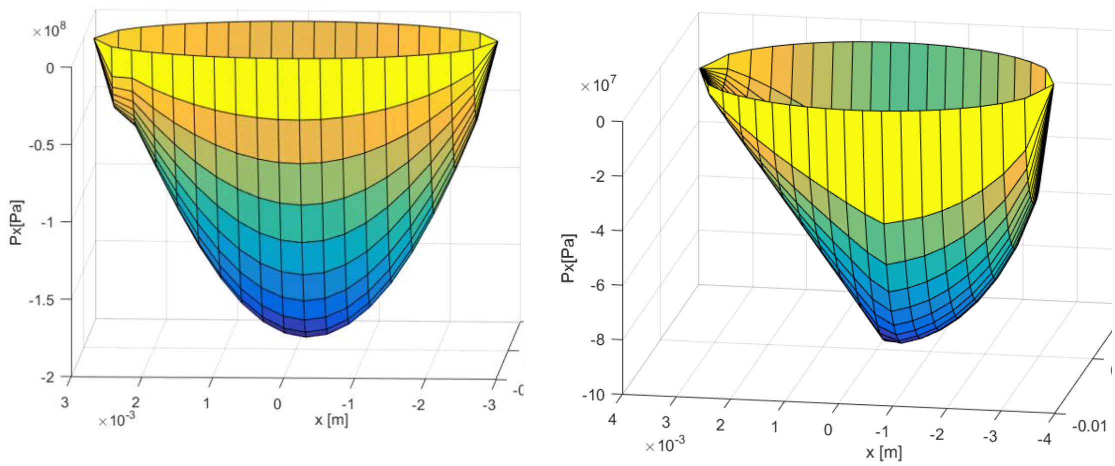

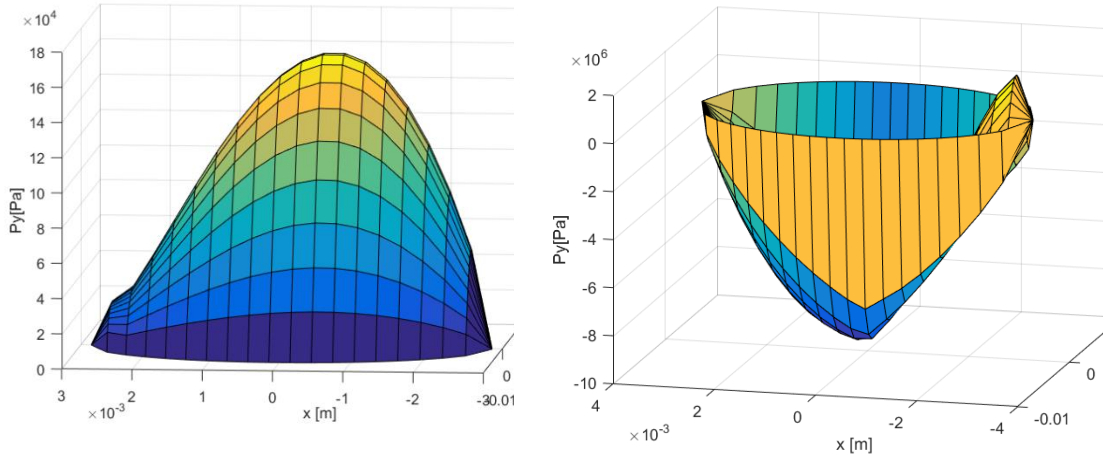

Figure 11. Comparison of the tangential pressures p_{tx} and p_{ty} for the first wheelset in a pure sliding condition (on the left) and in a partial adherence condition (on the right)

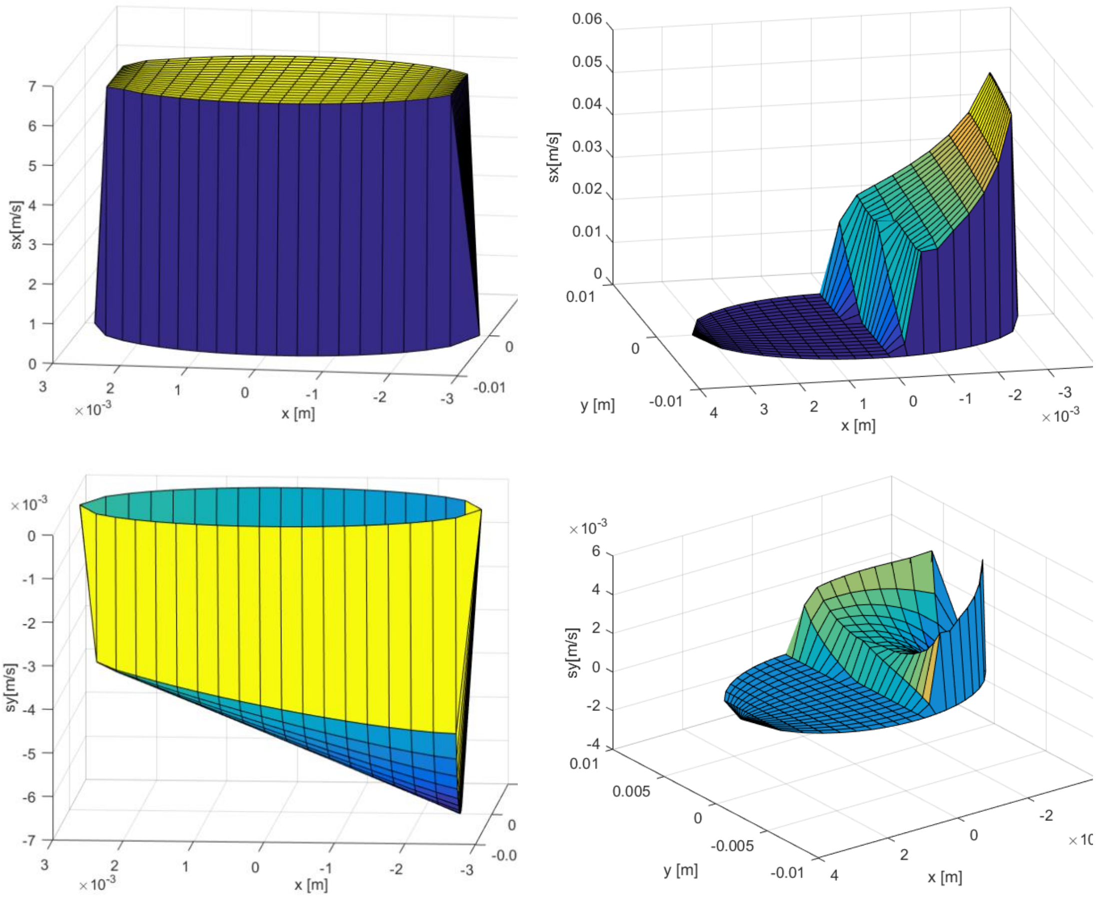

Figure 12. Comparison of the local sliding s_x , s_y for the first wheelset in a pure sliding condition (on the left) and in a partial adherence condition (on the right)

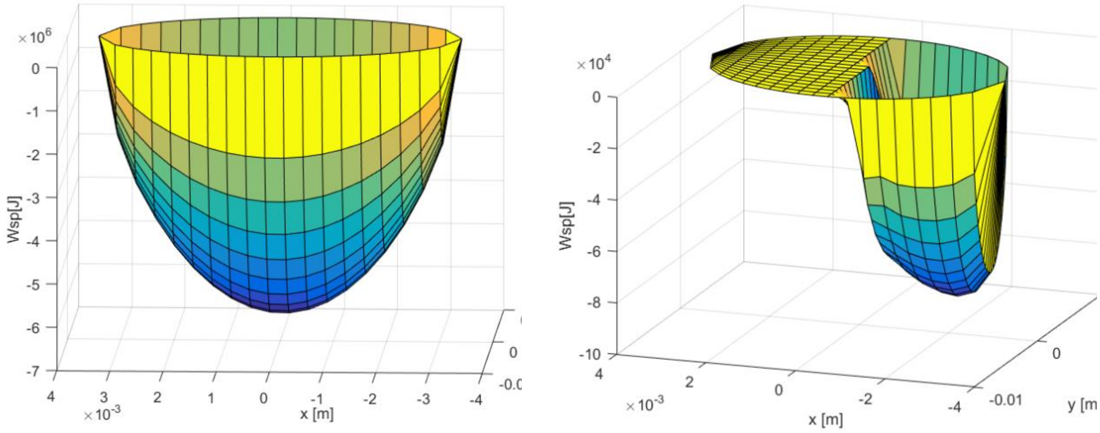

Figure 13. Comparison of the dissipated energy W_{sp} for the first wheelset in a pure sliding condition (on the left) and in a partial adherence condition (on the right)

7. Conclusions

In this work the authors presented a model aimed to describe degraded adhesion conditions at the wheel-rail contact interface in railway vehicle dynamics. The new approach is suitable for multibody applications and assures high computational performances, making possible the direct online implementation of the degraded adhesion model within more general vehicle multibody models. The new model is based on the main phenomena characterising the degraded adhesion, such as the energy dissipation at the contact interface, the consequent cleaning effect and the resulting adhesion recovery due to the removal of external unknown contaminants. Since most of the physical characteristics of the contaminants are totally unknown in practice, the new approach minimizes the number of hardly measurable physical quantities required by the model.

The adhesion model has been validated thanks to experimental data provided by Trenitalia S. p. A. coming from on-track tests performed in Velim (Czech Republic) with the railway vehicle UIC-Z1. The tests have been carried out on a straight railway track under degraded adhesion conditions with a vehicle equipped with a Wheel Slide

Protection (WSP) system. Many important developments are scheduled for the future. Some improvements of the model will be taken into account, and finally the new degraded adhesion model will be applied to the study of the railway vehicle dynamics and of the wheel-rail contact on generic railway tracks and networks. This way, some important topics such as the profile evolution due to wear, the profile optimization and the development of innovative railway bogies will be further investigated.

Acknowledgements

The authors would like to thank Trenitalia S.p.A. for supplying the technical data and the experimental data related to the braking tests under degraded adhesion conditions needed for the model validation.

References

1. Polach: Creep forces in simulations of traction vehicles running on adhesion limit. Wear 258, 992-1000, 2005
2. Auciello, J., Meli, E., Falomi, S., Malvezzi, M.: Dynamic simulation of railway vehicles: wheel/rail contact analysis. Veh. Syst. Dyn. 47, 867–899 (2009)
3. Falomi, S., Malvezzi, M., Meli, E.: Multibody modeling of railway vehicles: innovative algorithms for the detection of wheel–rail contact points. Wear 271(1–2), 453–461 (2011)
4. E. Meli, S. Falomi, M. Malvezzi, A. Rindi: Determination of wheel rail contact points with semianalythic methods. Multibody System Dynamics 20 Issue 4, 327-358, 2008.
5. Shabana, A., Tobaa, M., Sugiyama, H., Zaazaa, K.: On the computer formulations of the wheel/rail contact problem. Nonlinear Dyn. 40, 169–193 (2005) 39.
6. Shabana, A.A. , Zaaza, K.E. , Escalona, J.L., Sang,J.R. : Development of elastic force model for wheel/rail contact problems. J. Sound Vib. 269, 295–325 (2004)
7. Kalker, J.: Three-Dimensional Elastic Bodies in Rolling Contact. Kluwer Academic, Norwell (1990)

8. Antoine, J., Visa, C., Sauvey, C., Abba, G.: Approximate analytical model for hertzian elliptical contact problems. J. Tribol. 128, 660–664 (2006
9. Ayasse, J., Chollet, H.: Determination of the wheel–rail contact patch in semi-hertzian conditions. Veh. Syst. Dyn. 43, 161–172 (2005)
10. Dukkipati, R., Amyot, J.: Computer Aided Simulation in Railway Dynamics. Dekker, New York, USA (1988)
11. Esveld, C.: Modern Railway Track. Delft University of Technology, Delft, Netherlands (2001)
12. Johnson, K.: Contact Mechanics. Cambridge University Press, Cambridge, UK (1985)
13. Kalker,J.J.:A fast algorithm for the simplified theory of rolling contact. Veh. Syst. Dyn. 11,1–13(1982)
14. Ignesti, M., Malvezzi, M., Marini, L., Meli, E., Rindi, A.: Development of a wear model for the prediction of wheel and rail profile evolution in railway systems. Wear 284–285, 1–17 (2012)
15. Iwnicki, S. : Handbook of Railway Vehicle Dynamics. Taylor and Francis, London (2006)
16. S. Margheri, M. Malvezzi, E. Meli, A. Rindi: An innovative wheel rail contact model for multibody applications. Wear 271 Issue 1, 462-471, 2011
17. Polach, O.: A fast wheel–rail forces calculation computer code. Veh. Syst. Dyn. 33, 728–739 (1999)
18. Pombo, J. , Silva, A. : A new wheel–rail contact model for railway dynamics. Veh. Syst. Dyn. 45, 165–189 (2007)
19. E. Meli, A. Ridolfi: An innovative wheel–rail contact model for railway vehicles under degraded adhesion condition .Multibody System Dynamics March 2015, Volume 33, Issue 3, pp 285–313
20. Arias-Cuevas, O., Li, Z., Lewis, R.: A laboratory investigation on the influence of the particle size and slip during sanding on the adhesion and wear in the wheel–rail contact. Wear 271, 14–24 (2011)
21. Arias-Cuevas, O., Li, Z., Lewis, R., Gallardo-Hernandez, E.: Rolling–sliding laboratory tests of friction modifiers in dry and wet wheel–rail contacts. Wear 268, 543–551 (2010)

22. Chen, H., Ban, T., Ishida, M., Nakahara,T.: Experimental investigation of influential factors on adhesion between wheel and rail under wet conditions. Wear 265, 1504–1511 (2008)
23. Descartes, S., Desrayaud, C., Niccolini, E., Berthier, Y.: Presence and role of the third body in a wheel– rail contact. Wear 258, 1081–1090 (2005)
24. Eadie, D., Kalousek, J., Chiddick, K.: The role of high positive friction (hpf) modifier in the control of short pitch corrugations and related phenomena. Wear 253, 185–192 (2002)
25. Gallardo-Hernandez, E., Lewis, R.: Twin disc assessment of wheel/rail adhesion. Wear 265, 1309–1316 (2008)
26. Niccolini, E., Berthier, Y.: Wheel–rail adhesion: laboratory study of "natural" third body role on locomotives wheels and rails. Wear 258, 1172–1178 (2005)
27. Wang, W., Zhang, H., Wang, H., Liu, Q., Zhu, M.: Study on the adhesion behavior of wheel/rail under oil, water and sanding conditions. Wear 271, 2693–2698 (2011)
28. Allotta, B., Conti, R., Malvezzi, M., Meli, E., Pugi, L., Ridolfi, A.: Numerical simulation of a HIL full scale roller-rig model to reproduce degraded adhesion conditions in railway applications. In: European Congress on Computational Methods in Applied Sciences and Engineering (ECCOMAS 2012), Austria (2012)
29. Voltr, P., Lata, M., Cerny, O.: Measuring of wheel–rail adhesion characteristics at a test stand. In: XVIII International Conference on Engineering Mechanics, Czech Republic (2012)
30. Zhang, W., Chen, J., Wu, X., Jin, X.: Wheel/rail adhesion and analysis by using full scale roller rig. Wear 253, 82–88 (2002)
31. M. Malvezzi, E. Meli, S. Falomi: Multibody modeling of railway vehicles: innovative algorithms for the detection of wheelrail contact points. Wear 271 Issue 1, 453-461, 2011
32. Allotta, B., Meli, E., Ridolfi, A., & Rindi, A. (2014). Development of an innovative wheel–rail contact model for the analysis of degraded adhesion in railway systems. Tribology International, 69, 128-140.
33. Meli, E., Pugi, L., & Ridolfi, A. (2014). An innovative degraded adhesion model for multibody applications in the railway field. Multibody System Dynamics, 32(2), 133-157.

34. Allotta, B., Malvezzi, M., Pugi, L., Ridolfi, A., Rindi, A., Vettori, G.: Evaluation of odometry algorithm performances using a railway vehicle dynamic model. Veh. Syst. Dyn. 50(5), 699–724 (2012)
35. TrenitaliaSpA: UIC-Z1 coach. Internal report of Trenitalia, Rome, Italy (2000)
36. TrenitaliaSpA: WSP systems. Internal report of Trenitalia, Rome, Italy (2006)